Output Power and Gain Monitoring in RF CMOS Class A Power Amplifiers by Thermal Imaging

X. Perpiñá, F. Reverter, J. León, E. Barajas, M. Vellvehi, X. Jordà, J. Altet

***Abstract*—The viability of using off-chip single-shot imaging techniques for local thermal testing in integrated Radio Frequency (RF) power amplifiers (PA's) is analyzed. With this approach, the frequency response of the output power and power gain of a Class A RF PA is measured, also deriving information about the intrinsic operation of its transistors. To carry out this case study, the PA is heterodynally driven, and its electrical behavior is down converted into a lower frequency thermal field acquirable with an InfraRed Lock-In Thermography (IR-LIT) system. After discussing the theory, the feasibility of the proposed approach is demonstrated and assessed with thermal sensors monolithically integrated in the PA. As crucial advantages to RF-testing, this local approach is non-invasive and demands less complex instrumentation than the mainstream commercially available solutions.**

***Index Terms*— Output Power and Gain Measurement, RF CMOS power amplifiers, Local thermal testing, thermal sensors, Infrared Thermography, Heterodyne driving.**

I. INTRODUCTION

WIRELESS transceivers integration in Systems on Chip (SoC's) has represented an impressive breakthrough in Radio Frequency (RF) communications. This achievement has resulted from making compatible with the Complementary Metal-Oxide-Semiconductor (CMOS) fabrication process, the implementation of RF Power and Low Noise Amplifiers (PA and LNA), mixers, voltage local oscillator, and RF passive components (e.g., capacitors, inductors, and resistors) [1], [2]. In this field, some challenges are related to non-mature fabrication technology issues (e.g., environmental electrical changes or process variability) [1]. Others deal with reducing SoC power and area consumption, while keeping the same wireless coverage and data rate capacity [1], [3], [4]. All them are posing several constraints in SoC design, testability, and manufacturability, especially to meet the required output power and power gain response in linear RF PA's (mainly Class A [5]). Obviously, all this compromises the SoC performance and dependability [1], [3], [4]. Thus, great efforts are being invested to improve PA's and SoC debugging strategies [1], [2], [3], [4]. In this respect, the measurement of Figures of Merit (FoM's) in any SoC internal node is crucial to identifying the responsible (i.e., transistor, component, or block) for any PA FoM degradation [1], [6]. In fact, correlating FoM's spectrum with transistors operation regimes is an unexplored field of study to locally face such concerns. Currently, FoM's are being measured at RF Integrated Circuit (RF-IC) or block level using commercial systems (e.g., virtual network or Spectrum Analyzers, SA), or integrating monitor circuits (MIC's), but without accessing to all SoC internal nodes [2], [6], [7], [8]. In the former case, FoM's are layout averaged and very sensitive to node's equivalent impedance, requiring frequency-adapted pads. [9] Conversely, MIC design requests for an optimum layout placement, testability, and manufacturability, [10], [11] without any SoC performance degradation [12], [13]. Although sensing non-electrical variables mainly addresses such demands, the MIC placement is still unsolved [14], [15], [16].

To cover all such needs, off-chip single-shot imaging of non-electrical observables (e.g., temperature or strain) is very promising [17], [18], [19], [20], as non-invasive testability of all internal nodes is assured while the RF-IC is under regular operation [21]. Thanks to the use combined of an RF block frequency-modulated driving and a mixer-like approach, electrical information is down converted from a higher to a lower frequency observable measured by following lock-in procedures (heterodyne technique) [20], [22], [23]. In contrast to point-by-point scanning, single-shot enables all image pixels acquisition at once, thus fastening large areas inspection and reducing SoC costs [10]. In spite of such advantages, the FoM's spectrum in RF-IC's has still not been performed by single-shot imaging, neither a rigorous feasibility study reported. First experiments have been focused on hot spot monitoring with scanning methodologies [24] or MIC's [25] to extract FoM calibration-free parameters in LNA's and PA's (i.e., power gain central frequency [24] or 3dB bandwidth [24], [25]). In such works, temperature sensing has offered a clear gain to

Manuscript received Month xx, 2xxx; revised Month xx, xxxx; accepted Month x, xxxx. This work was supported in part by the Spanish Ministries of Science and Innovation, and Economy and Competitiveness (under the research programs: TEC2013-45638-C3-2-R, SMARTCELLS TEC2014-51903-R, Ramón y Cajal RYC-2010-07434), as well as by the regional government of the Generalitat de Catalunya (2017 SGR 1384).

X. Perpiñà, J. León, M. Vellvehi, and X. Jordà are with the Institut de Microelectrònica de Barcelona, IMB-CNM (CSIC) Campus UAB, 08193 Cerdanyola, Spain (e-mail: xavier.perpinya@imb-cnm.csic.es; javier.leon@imb-cnm.csic.es; miquel.vellvehi@imb-cnm.csic.es; xavier.jorda@imb-cnm.csic.es).

F. Reverter, E. Barajas, and J. Altet are with the Department of Electronic Engineering, Universitat Politècnica de Catalunya (UPC) − BarcelonaTech, 08034 Barcelona, Spain (e-mail: ferran.reverter@upc.edu; enrique.barajas@upc.edu; josep.altet@upc.edu)

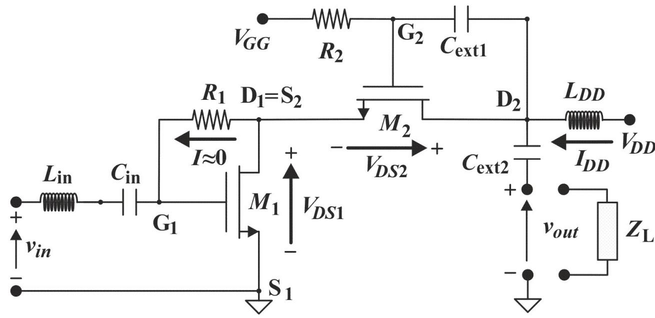

Fig. 1. Schematic of the analyzed PA indicating the DC biasing.

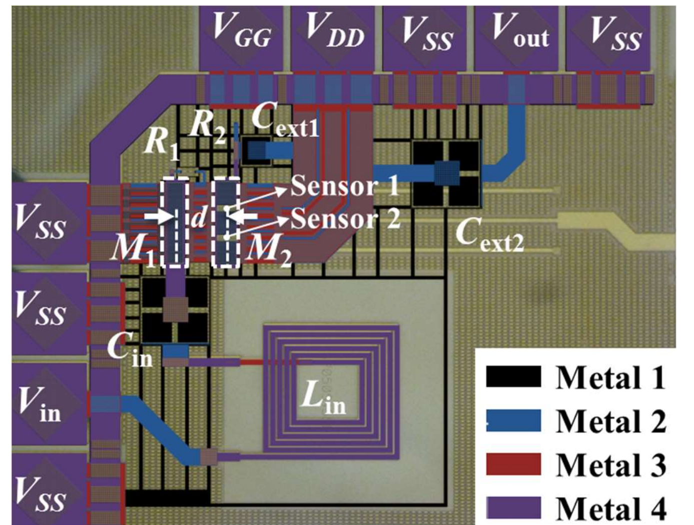

Fig. 2. PA layout highlighting the input/output pads and pinout, main interconnection tracks (power supply and output), active (M_1 and M_2, at a distance *d*) and passive (C_{in}, L_{in}, $C_{ext,1}$ and $C_{ext,2}$) components. All levels of interconnecting metals (made of aluminum) are also shown.

implement heterodyne strategies over other solutions [18], [22], [23], [26], as the power dissipated by transistors or other IC parts inherently mixes current and voltage signals by Joule effect. To acquire in SoC's single-shot thermal images, InfraRed (IR) thermography is a good candidate, as frequency-modulated hot spots can be studied by lock-in detection (InfraRed Lock-In Thermography, IR-LIT) [27], [28], [29] with the following profits [30], [31]. The influence of either other spectral component of temperature different to the modulation frequency (i.e., DC or other Fourier components) or external noise sources are suppressed. Besides, weak heat sources below 1 mºC are detected with enough lateral resolution [30] under heterodyne driving [19], [22], [32].

As a main innovation in this scenario, this work aims at exploring the feasibility of using IR-LIT to monitor the frequency response (from 100 MHz up to 2 GHz) of some FoM's in RF-IC's. Concretely, this is applied to extract the frequency response of both the output power and the power gain in a Class A RF PA's with a different value of central frequency. In addition, the thermal imaging results are also employed to detect local electrical information at transistor level, e.g., the non-constant transconductance of the cascode transistor of the RF-PA. To check IR-LIT results, a thermal sensor has been monolithically integrated in the PA chip. In relation to such targets, this paper is organized as follows. Section II presents the analyzed RF PA topology, the theoretical basis to measure both the output power and power gain frequency response, and deduce the used calibration law. Section III details the experimental conditions, whereas IR-LIT results are discussed and verified with the on-chip sensor in Section IV. Finally, the conclusions are drawn in Section V.

II. FoM's Thermal Measurement in Class A RF PA's

A. Class A PA description and layout

A cascode Class A PA, with an isolated DC output and L-C band frequency tuning (see schematic in Fig. 1), has been selected as a proof-of-concept due to its extensive use and benefits. In comparison with other single stages, cascode topology presents [33] a higher power gain, bandwidth [5], [34], and output impedance, with a lower consumption [35]. Fig. 2 depicts the PA physical layout of the schematic shown in Fig. 1, with the thermal sensors integrated with the PA in the same chip for IR-LIT results assessment. The PA and integrated sensors have been fabricated with a 0.35 µm 2P4M (2 levels of polysilicon, 4 levels of metal) CMOS technology of AMS (AustriaMicroSystems) in 725 µm thick wafers, with all geometrical and nominal values of Fig. 1 detailed in Table I. As a main PA design purpose, this test vehicle has been conceived unconditionally stable without any further performance optimization. As for on-chip temperature monitoring, two thermal sensors based on a diode-connected n-type MOSFET topology [36] have been monolithically integrated within the interdigitated structure of M_2 (see Fig. 2). M_2 was selected as it adapts the impedance between M_1 and Z_L, and ensures a lower impact on PA amplification than M_1. According to [37], the sensitivity of such thermal sensors is enhanced when: they are biased in strong inversion with a drain to source current of 20 µA and their channel width (*W*)-length (*L*) aspect ratio is set for 1.5/24. The dynamic equivalent resistance of this device and the parasitic capacitance ensure that its 3-dB cut-off frequency is higher than 160 kHz, allowing the thermal acquisition in the studied frequency ranges [36], [38].

TABLE I
RF-PA Layout, Components Data and Small-Signal Parameters

Component/ Dimensions	Value by Design	Small-Signal/ Layout Data	Value by Design
R_1 (Ω)	6428	C_{gs1} (pF)	3.60
R_2 (Ω)	6428	C_{dg1} (fF)	370
C_{in} (pF)	5	g_{m1} (mS)	135
C_{ext1}(pF)	1	g_{ds1} (mS)	3.20
C_{ext2} (pF)	5	C_{gs2} (pF)	2.46
L_{in} (nH)	12.2	C_{dg2} (fF)	258
L_{DD} (nH)	19.2	g_{m2} (mS)	135
W_1 (µm)	1159	g_{ds2} (mS)	7.20
L_1 (µm)	0.5	M_1 Fingers	61
W_2 (µm)	1173	M_2 Fingers	51
L_2 (µm)	0.5	*d* (µm)	48.5

B. PA homodyne driving and FoM's electrical testing

Fig. 3 shows its small-signal equivalent circuit, and Table I summarizes the value of its elements, where $g_{ds1} = r_{ds1}^{-1}$ and

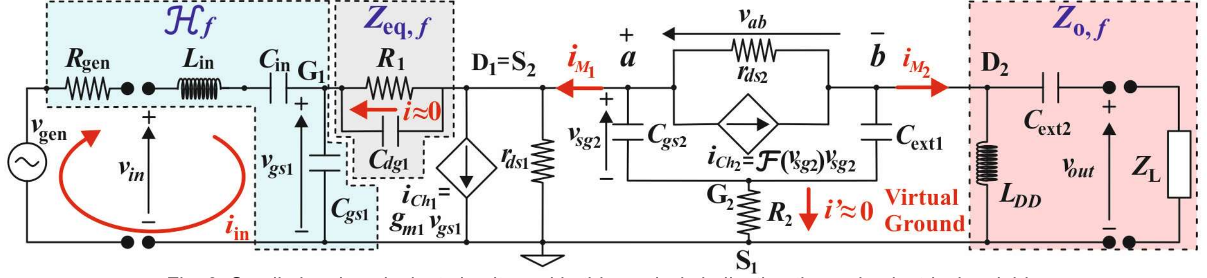

Fig. 3. Small-signal equivalent circuit used in this analysis indicating the main electrical variables.

$g_{ds2} = r_{ds2}^{-1}$. $\mathcal{H}_f$, $Z_{\text{eq},f}$, and $Z_{\text{o},f}$ are the equivalent impedances of the elements within the colored areas of Fig. 3, indicating its frequency dependence as a subscript f. Concretely, $\mathcal{H}_f$ and $Z_{\text{o},f}$ fix both the PA output spectral response and central frequency $f_{\text{c,G}}$. In contrast, R_1, $Z_{\text{eq},f}$, and R_2 values are large (see Table I) to force $i \approx i' \approx 0$, provide the DC biasing, and apply the virtual ground in G_2. In Fig. 3, the load ($Z_{\text{L},f}$) is an impedance instead of a pure resistor (e.g., antenna) to contemplate eventual parasitics ($Z_{\sigma,f}$). As notation criteria, electrical variables X (i.e., voltage, current, or dissipated power) are expressed according to Euler formula and its frequency dependence pointed out as a subscript f, $X_f = |X_f|\, e^{j(2\pi f t \quad X_f)}$, where $|X_f|$ and θ_{X_f} are the amplitude and phase lag of X_f; whereas their real part ($\text{Re}[X_f]$) writes as $\text{Re}[X_f] = |X_f| \cos(2\pi f t + \theta_{X_f})$.

To access to the potential of the imaging approach proposed for RF-testing, the PA output power and gain are inferred when the input power ($P_{\text{in},f}$) is below the 1-dB Compression Point (CP) at $f_{\text{c,G}}$. This sets the PA under linear regime with a constant transconductance g_{m1} in M_1, whereas the M_2 transconductance ($\mathcal{F}(v_{sg2,f})$) is modelled as $\mathcal{F}(v_{sg2,f}) = g_{m2} - K_2 v_{sg2,f}$ ($K_2 > 0$). This considers short channel and vertical field effects induced by V_{DD} and V_{GG} bias [39], [40]. By expressing $v_{sg2,f}$ in terms of $v_{\text{gen},f}$ (see Fig. 3), $v_{sg2,f}$ writes as:

$$v_{sg2,f} = \left(\frac{-A_f}{\left(1+\sqrt{1+A_f B_f\ v_{\text{gen},f}}\right)}\right) v_{\text{gen},f} = G_f(v_{\text{gen},f}) v_{\text{gen},f} \quad (1)$$

where A_f and B_f are related with the circuit elements depicted in Fig. 3 and simplified according to Table I values as follows:

$$A_f = \frac{2\, g_{m1}\mathcal{H}_f}{g_{m2}+g_{ds1}+\frac{g_{ds2}}{(g_{m2}+g_{ds2})}\delta Z_f} \approx \frac{2\, g_{m1}\mathcal{H}_f}{g_{m2}} \quad (2)$$

$$B_f = \frac{2\, K_2\left(1-(Z_{\text{o},f} \| r_{ds2})\right)}{g_{m2}+g_{ds1}+\frac{g_{ds2}}{(g_{m2}+g_{ds2})}\delta Z_f} \approx \frac{2\, K_2}{g_{m2}} \quad (3)$$

where $\delta Z_f = g_{m2}^{-1} - (Z_{\text{o},f} \parallel r_{ds2})$. Therefore, $v_{ab,f}$ and $v_{\text{out},f}$ relate to $v_{sg2,f}$ as:

$$v_{ab,f} = \left[1 - (Z_{\text{o},f} \parallel r_{ds2})(g_{m2} - K_2 v_{sg2,f} + g_{ds2})\right] v_{sg2,f}, \quad (4)$$

$$v_{\text{out},f} = \frac{Z_{\text{L},f}(Z_{\text{o},f} \| r_{ds2})(g_{m2} - K_2 v_{sg2,f} + g_{ds2})}{Z_{C_{\text{ext2},f}} + Z_{\text{L},f}} v_{sg2,f}\ . \quad (5)$$

As $g_{m2}^2 \gg K_2 g_{m1} \mathcal{H}_f v_{\text{gen},f}$ in (1), $G_f(v_{\text{gen},f})$ allows its Taylor series expansion around the amplitude of $v_{\text{gen},f}$ ($|v_{\text{gen},f}|$), applying the following zero order approximation:

$$v_{sg2,f} \approx G_f(|v_{\text{gen},f}|)\, v_{\text{gen},f}\ . \quad (6)$$

Usually, the power delivered to $Z_{\text{L},f}$ ($P_{\text{out},f}$) is determined with RF electrical systems (e.g., SA) by measuring $v_{\text{out},f}$ using heterodyne approaches, and performing:

$$P_{\text{out},f} = \text{Re}\left[(v_{\text{out},f})^2 / Z_{\text{L},f}\right], \quad (7)$$

where $Z_{\text{L},f}$ is a real load R_{L} with a parasitic impedance $Z_{\sigma,f}$. When the PA is driven with a single tone voltage waveform (homodyne driving), i.e., $v_{\text{gen},f_0} = v_0 \sin(2\pi f_0 t)$, the power gain Γ_{hom,f_0} (i.e., $\text{Re}[P_{\text{out},f_0}/P_{\text{in},f_0}]$) is inferred from (1)-(7) as:

$$\Gamma_{\text{hom},f_0} = \text{Re}\left[\left(\mathcal{L}_{f_0} - \mathcal{J}_{f_0} G_{f_0}(v_0)\, v_{\text{gen},f_0}\right)^2 \left[G_{f_0}(v_0) v_0\right]^2 R_{\text{in}}\right], \quad (8)$$

where $R_{\text{in}} = R_{\text{gen}} = \text{Re}[Z_{\text{L},f_0}] = R_{\text{L}} = 50\ \Omega$, $\text{Im}[Z_{\text{L},f_0}] = Z_{\sigma,f_0} \approx 0$,

$$\mathcal{L}_{f_0} = \frac{Z_{\text{L},f_0}(Z_{\text{o},f_0} \| r_{ds2})(g_{m2} + g_{ds}\ )}{Z_{C_{\text{ext2},f_0}} + Z_{\text{L},f_0}}, \quad (9)$$

and

$$\mathcal{J}_{f_0} = \frac{Z_{\text{L},f_0}(Z_{\text{o},f_0} \| r_{ds2}) K_2}{Z_{C_{\text{ext2},f_0}} + Z_{\text{L},f_0}}. \quad (10)$$

C. PA heterodyne driving and FoM's thermal testing

When $v_{\text{gen}} = v_{\text{gen,het}} = v_0/2\,[\sin(2\pi f_1 t) + \sin(2\pi f_2 t)]$ with f_1, $f_2 \approx f_0$ and $\Delta f = f_1 - f_2 \ll f_1$, f_2 ($v_{\text{gen,het}}$, heterodyne driving), the power dissipated by M_1 and M_2 has spectral components at Δf (i.e., $P_{M_1,\Delta f}$, $P_{M_2,\Delta f}$), originating a thermal field detectable at this frequency [22]. Under this driving, $P_{M_1,\Delta f}$, $P_{M_2,\Delta f}$ and the power delivered to Z_{L} at f_k (P_{Z_{L},f_k}, where k=1, 2) write as:

$$P_{M_1,\Delta f} = \text{Re}\left[\sum_{k \neq j}^{2} i_{M_1,f_k} v_{ds1,f_j}\right] =$$
$$= \text{Re}\left[\sum_{k \neq j}^{2} (i_{Ch_1,f_k} + v_{sg\ \ ,f_k}\, g_{ds}\ \ ) v_{sg2,f_j}\right] =$$

$$= -\mathrm{Re}\left[\sum_{k\neq j}^{2}\left[\frac{g_{m1}\mathcal{H}_{f_k}}{G_{f_k}(v_0/2)} - g_{ds1}\right] v_{sg2,f_j}^2\right], \qquad (11)$$

$$P_{M_2,\Delta f} = \mathrm{Re}\left[\sum_{k\neq j}^{2} -i_{M_2,f_k} v_{ds2,f_j} + V_{DS2} i_{M_2,\Delta f}^{nl} + I_{DD} v_{ab,\Delta f}^{\mathrm{nl}}\right] =$$
$$= \mathrm{Re}\left[\sum_{k\neq j}^{2}\left(i_{Ch_2,f_k} + v_{ab,f_k} g_{ds2}\right) v_{ab,f_j} + V_{DS2}\, i_{M_2,\Delta f}^{nl}\right.$$
$$\left. + I_{DD} v_{ab,\Delta f}^{\mathrm{nl}}\right] \approx \mathrm{Re}\left[\sum_{k\neq j}^{2}\left(g_{m2}^2 \delta Z_{f_k} + k_2^2 v_{sg2,f_k}^2\right) v_{sg2,f_j}^2\right], \qquad (12)$$

$$P_{Z_{\mathrm{L}},f_k} = \mathrm{Re}\left[\left(v_{\mathrm{out},f_k}\right)^2 / Z_{\mathrm{L},f_k}\right], \qquad (13)$$

where the subscript j refers to 1 or 2 and the superscript "nl" indicates the $v_{sg2,\Delta f}^2$-terms introduced by $\mathcal{F}(v_{sg}\ )$ in $i_{M_2,\Delta f}$ and $v_{ab,\Delta f}$. Node relations $v_{ds1,f_k} = v_{sg2,f_k}$, $i_{M_1,f_k} = i_{Ch_1,f_k} + v_{sg2,f_k}\, g_{ds1}$, $v_{ds2} = -v_{ab}$, and $i_{M_2,f_k} = i_{Ch_2,f_k} + v_{ab,f_k}\, g_{ds2}$ deduced from Fig. 3 have been used to infer (11)-(12). As in II.B, P_{Z_{L},f_k} is quantified by measuring v_{out,f_k} with an SA.

To write in terms of v_{sg2,f_k}, the temperature spectral component generated by M_1 at Δf for any location on top of the die at a distance r_{M_1} from M_1 [$\Delta T_{M_1,\Delta f}(r_{M_1})$], (6) is accounted, i.e., $v_{sg2,f_k} \approx G(|v_{\mathrm{gen},f_k}|)\, v_{\mathrm{gen},f_k}$ with $|v_{\mathrm{gen},f_k}| = \frac{v_0}{2}$. Then, since $\Delta T_{M_1,\Delta f} \propto P_{M_1,\Delta f}$, $\Delta T_{M_1,\Delta f}$ is related with v_{sg2,f_k} as [41]:

$$\Delta T_{M_1,\Delta f}(r_{M_1}) = -\left|\frac{g_{m1}\mathcal{H}_{f_k}}{G_{f_k}(v_0/2)} - g_{ds1}\right| \left|v_{sg2,f_k}\right|^2 \cos(\theta_{v_{sg2,f_k}})$$
$$\times \mathcal{T}(r_{M_1}, \Delta f) \cos\left[(2\pi\Delta f)t - \phi_{\mathcal{T}}(r_{M_1}, \Delta f)\right] \qquad (14)$$

where $\mathcal{T}(r_{M_1}, \Delta f)$ is the transfer thermal function of M_1, with an amplitude $|\mathcal{T}(r_{M_1}, \Delta f)|$ and phase lag $\phi_{\mathcal{T}}(r_{M_1}, \Delta f)$. $\theta_{v_{sg2,f_k}}$ provides the electrical phase lag between i_{M_1,f_k} and v_{sg2,f_k}. Besides, $|v_{sg2,f_k}| \approx |v_{sg\ ,f_j}|$ and $\theta_{v_{sg2,f_k}} \approx \theta_{v_{sg2,f_j}}$ are assumed as $f_1, f_2 \approx f_0$ due to $\Delta f \ll f_1, f_2$. In this analysis, $\cos(\theta_{v_{sg2,f_k}})$ is required to relate $|\Delta T|_{M_1,\Delta f}(\vec{r}_{M_1})$ with $|v_{sg2,f_k}|$, as only $\mathrm{Re}[P_{M_1,\Delta f}]$ dissipates into heat. Actually, $\cos(\theta_{v_{sg2,f_k}}) \approx -1$ due to the fact that $i_{M_1,f_k} > 0$ and $v_{ds1,f_k} < 0$, as cascode topology inverts the sign of $v_{\mathrm{gen},f}$ in both $v_{\mathrm{out},f}$ and $v_{ds1,f}$. [33, 35] Thus, $|v_{sg2,f_k}|$ is expressed as:

$$|v_{sg2,f_k}| = \sqrt{\frac{|\Delta T|_{M_1,\Delta f}(r_{M_1})}{|\mathcal{T}(r_{M_1},\Delta f)|}\left|\frac{g_{m1}\mathcal{H}_{f_k}}{G_{f_k}(v_0/2)} - g_{ds}\ \right|^{-1}}. \qquad (15)$$

To link the output FoM's with $\Delta T_{M_1,\Delta f}(r_{M_1})$, its relationship with $|P_{Z_{\mathrm{L}},f_k}|$ and $|P_{\mathrm{out},f_0}|$ is firstly derived. According to (5), (13), and (15), $|P_{Z_{\mathrm{L}},f_k}|$ depends on $|\Delta T|_{M_1,\Delta f}(r_{M_1})$ as:

$$|P_{Z_{\mathrm{L}},f_k}| = a\, |\Delta T|_{M_1,\Delta f}(r_{M_1}) - b\, \left(|\Delta T|_{M_1,\Delta f}(r_{M_1})\right)^{3/2}$$
$$+ c\, \left(|\Delta T|_{M_1,\Delta f}(r_{M_1})\right)^2, \qquad (16)$$

where a, b, and c can be expressed in terms of the small-signal parameters pointed out in Fig. 3 and Table I as follows:

$$a = \frac{(g_{m2}+g_{ds2})^2 \left|Z_{\mathrm{o},f_k} \| r_{ds2}\right|^2 \left|\frac{g_{m1}\mathcal{H}_{f_k}}{G_{f_k}(v_0/2)} - g_{ds1}\right|^{-1}}{\left|Z_{C_{\mathrm{ext2},f_k}} + Z_{\mathrm{L},f_k}\right|^2 |\mathcal{T}(r_{M_1},\Delta f)|}, \qquad (17)$$

$$b = \frac{2K_2(g_{m2}+g_{ds2}) \left|Z_{\mathrm{o},f_k} \| r_{ds}\ \right|^2 \left|\frac{g_{m1}\mathcal{H}_{f_k}}{G_{f_k}(v_0/2)} - g_{ds1}\right|^{-3/2}}{\left|Z_{C_{\mathrm{ext2},f_k}} + Z_{\mathrm{L},f_k}\right|^2 |\mathcal{T}(r_{M_1},\Delta f)|^{3/2}}, \qquad (18)$$

$$c = \frac{K_2^2 \left|Z_{\mathrm{o},f_k} \| r_{ds2}\right|^2 \left|\frac{g_{m1}\mathcal{H}_{f_k}}{G_{f_k}(v_0/2)} - g_{ds}\ \right|^{-2}}{\left|Z_{C_{\mathrm{ext2},f_k}} + Z_{\mathrm{L},f_k}\right|^2 |\mathcal{T}(r_{M_1},\Delta f)|^2}. \qquad (19)$$

In (18) and (19), b and c depend on K_2, and any non-linearity in M_2 is manifested in (16). Thus, a, b, and c can be identified by fitting methods taking them constant (i.e., memoryless) for a given frequency range f_{ri} [42], [43]. $|P_{\mathrm{out},f_0}|$ depends on $|P_{Z_{\mathrm{L}},f_k}|$, as $|P_{\mathrm{out},f_0}| = 2|P_{Z_{\mathrm{L}},f_k}| + |P_{\mathrm{int}}|$, where $|P_{\mathrm{int}}|$ is a constant accounting for the spectral power set into other intermodulation products originated from a possible PA distortion in M_2.

To infer the power gain under heterodyne driving [$\Gamma_{\mathrm{het},f_k}$], P_{Z_{L},f_k} is written as a function of v_{gen,f_k} [i.e., $v_0/2\sin(2\pi f_k t)$, where $|v_{\mathrm{gen},f_k}| = v_0/2$], and $v_{sg\ ,f_k} \approx G_{f_k}(v_0/2) v_{\mathrm{gen},f_k}$. As $P_{\mathrm{in},f_k} = \left(v_{\mathrm{gen},f_k}\right)^2 / R_{\mathrm{gen}}$ and $\Gamma_{\mathrm{het},f_k} = \mathrm{Re}[P_{Z_{\mathrm{L}},f_k} / P_{\mathrm{in},f_k}]$, $|\Gamma_{\mathrm{het},f_k}|$ is described by:

$$|\Gamma_{\mathrm{het},f_k}| = \frac{|Z_{\mathrm{L},f_k}| \left|Z_{\mathrm{o},f_k} \| r_{ds2}\right|^2}{\left|Z_{C_{\mathrm{ext2},f_k}} + Z_{\mathrm{L},f_k}\right|^2} \left|G_{f_k}(v_0/2)\right|^2 \frac{R_{\mathrm{gen}}}{2} \mathcal{M}, \qquad (20)$$

where, as deduced from (14) and (15), $\mathcal{M}$ corresponds to:

$$\mathcal{M} = (g_{m2} + g_{ds}\ )^2 - 2\, K_2 (g_{m2} + g_{ds2})$$
$$\times \sqrt{\frac{|\Delta T|_{M_1,\Delta f}(r_{M_1})}{|\mathcal{T}(r_{M_1},\Delta f)|}\left|\frac{g_{m1}\mathcal{H}_{f_k}}{G_{f_k}(v_0/2)} - g_{ds1}\right|^{-1}}$$
$$+ K_2^2 \frac{|\Delta T|_{M_1,\Delta f}(r_{M_1})}{|\mathcal{T}(r_{M_1},\Delta f)|}\left|\frac{g_{m1}\mathcal{H}_{f_k}}{G_{f_k}(v_0/2)} - g_{ds1}\right|^{-1}, \qquad (21)$$

whereas $|\Gamma_{\mathrm{het},f_k}|$ relates with $|\Gamma_{\mathrm{hom},f_0}|$ as $|\Gamma_{\mathrm{hom},f_0}| = |\Gamma_{\mathrm{het},f_k}| + \left(|P_{\mathrm{int}}| / |P_{\mathrm{in},f_0}|\right)$ thanks to $f_k \approx f_0$ and $\Delta f \ll f_k$. Similarly to (16), $\mathcal{H}_{f_k}$, Z_{o,f_k}, $Z_{C_{\mathrm{ext2},f_k}}$ mainly fix the frequency response in (20); since g_{m2}, g_{m1}, $\mathcal{H}_{f_k}/G_{f_k}(\,v_0/2)$, K_2, g_{ds} , and g_{ds} are constants. Moreover, a fitting parameter can be consequently inferred for each term of $|\Delta T|_{M_1,\Delta f}(r_{M_1})$, as they are memoryless for a given f_{ri}. Thus, thermal monitoring not only allow FoM extraction ($|P_{\mathrm{out},f_0}|$ and $|\Gamma_{\mathrm{hom},f_0}|$), but also assessing transistor-related phenomena, since non-linear terms of $|\Delta T|_{M_1,\Delta f}(r_{M_1})$ appear in $|P_{Z_{\mathrm{L}},f_k}|$ and $|\Gamma_{\mathrm{het},f_k}|$ when $K_2 \neq 0$. Unfortunately, $|\Delta T|_{M_1,\Delta f}(r_{M_1})$ cannot be directly measured. Analogously to M_1, M_2 generates at any distance from its location (r_{M_2}), a surface thermal field $\Delta T_{M_2,\Delta f}(r_{M_2})$, which superposes to $\Delta T_{M_1,\Delta f}(r_{M_1})$. This gives rise to a total thermal

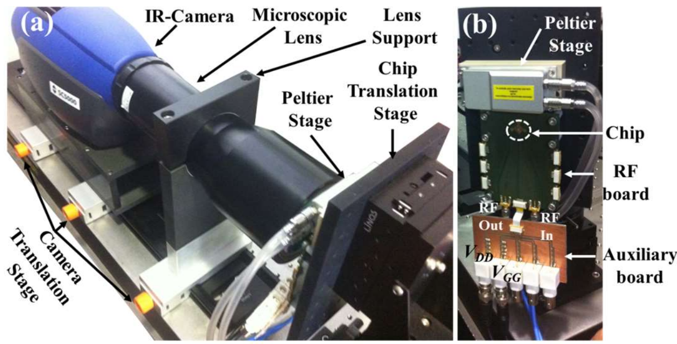

Fig. 4. (a) Experimental set-up with the IR-camera, a translation stage to focus the sample the location of the CUT. (b) Detail of the Peltier-thermo-regulated micro-positioning stage for measuring the amplifier.

field $\Delta T_{\mathrm{tot},\Delta f}(r_{M_1}, r_{M_2})$; i.e., $\Delta T_{\mathrm{tot},\Delta f}(r_{M_1}, r_{M_2}) = \Delta T_{M_1,\Delta f}(r_{M_1}) + \Delta T_{M_2,\Delta f}(r_{M_2})$. Therefore, $\Delta T_{\mathrm{tot},\Delta f}(r_{M_1}, r_{M_2})$ allows inferring $|P_{\mathrm{out},f_0}|$ and $|\Gamma_{\mathrm{hom},f_0}|$ from different die surface locations, after their calibration by fitting (16) and (20).

III. MATERIALS AND METHODS

A. PA packaging, biasing and driving

The die (area of 2.6×2.6 mm^2) has been attached to an RF board (chip on-board configuration) to reduce parasitic effects. An auxiliary board has been designed to DC bias the amplifier. To maximize the PA gain, V_{DD} = 3.3 V and V_{GG} = 3.2 V have been set, which induces a non-constant $\mathcal{F}(v_{sg2,f})$ in M_2. To demonstrate the viability of the imaging approach proposed for output FoM's measurement, the PA has been tuned at two $f_{\mathrm{c,G}}$'s: 620 MHz and 440 MHz. This $f_{\mathrm{c,G}}$ shift from 620 to 440 MHz has been carried out by soldering decoupling capacitors between V_{DD} (power supply) and V_{SS} (ground) tracks of the RF board to decrease their impedance at high frequencies, and hence, better adapt the RF power transfer. The PA has been heterodynally driven with an Agilent E4438C ESG Vector Signal Generator, while the PA output power has been measured with a FSQ26 Rohde & Schwarz SA. This output power is referred to as P_{out,f_0} or P_{Z_{L},f_k} when the PA is driven with one (homodyne) or two (heterodyne) sine waves. The total input power used in the experiments is comprised between -10 and -3 dBm, to keep it below the PA 1-dB CP at the $f_{\mathrm{c,G}}$ considered (0 dBm at 620 MHz,-2.5 dBm at 440 MHz [38]).

B. IR-LIT system, IR images acquisition and processing

The IR emission of the IC surface has been acquired with an IR imaging system. This piece of equipment is based on a FLIR SC5500 thermal camera operating in the waveband 3.7-5.0 μm. As a sensor, it has an InSb focal-plane array formed by 320×256 pixels, where each pixel sizes 30×30 μm^2, and cooled down with an integral stirling system. This camera allows acquiring images at a maximum frame rate (f_{R}) of 383 Hz at full frame image, and 31.7 kHz at subwindowing mode (64×8 pixels), featuring a low noise figure (Noise Equivalent Temperature Difference < 20 mK at 30ºC). To inspect the IC region of interest shown in Fig. 2, a FLIR microscope lens (G5X) has been used, presenting the following characteristics: a spatial resolution of 6 μm, an instantaneous field of view of 1.92×1.53 mm, a distance lens-object of 28.88 + 0.05 mm, a magnification of 5 + 5%, an F-number of 3 + 10% and a working distance of 18.60 mm. As for IR-LT measurements, the camera integrates a lock-in module (hardware correlation or detection) for on-line fast Fourier correlation with dedicated software (Flir Thesa), which fastens the thermal amplitude and phase lag determination.

The IR images have been acquired at f_{R} = 376 Hz and an integration time (t_{int}) of 450 μs, leading to 2.5×10^4 images processed at Δf. Such values are selected since they respectively are the highest f_{R}, the shortest t_{int}, and the smallest image number for which the camera signal to noise ratio is acceptable to perform a fast and proper lock-in processing, as demonstrated in [38]. In such images, the die surface IR emissivity (ε) has been corrected for each material without using any coating [44]. The real temperature amplitude maps have been obtained from the apparent ones by determining first the ε map. In this process, reflections coming from external sources are corrected, whereas in lock-in measurements, they are also suppressed as they do not present any spectral content at $f_{\mathrm{lock\text{-}in}} = \Delta f$. To compare off-chip with on-chip measurements, a pixel or an area-averaged value of $\Delta T_{\mathrm{tot},\Delta f}(r_{M_1}, r_{M_2})$ has been extracted at the location of the sensor and PA parts of interest n (referred to as $\Delta T^{\mathrm{n}}_{\mathrm{tot},\Delta f}$). The aim of area averaged measurements is to reduce the spatial noise in IR images introduced by the camera.

C. Δf selection for IR-LIT measurements

Several considerations have been taken into account for choosing an appropriate Δf value. First, a maximum (Δf_{max}) and minimum (Δf_{min}) value has been defined according to the following constraints. Δf must fall within the camera bandwidth (i.e., $\Delta f_{\mathrm{max}} < 1/(2\ t_{\mathrm{int}})$ [23]) and ensure the thermal measurements independence from the thermal boundary conditions. The latter is fulfilled by preventing that the diffusion of the heat spectral component at Δf reaches the die backside. This situation can be achieved under the thermally thick condition. Namely, considering the silicon thermal diffusivity (D_α, 85.47 mm^2/s [45]) and a given chip thickness (t_{chip}), then $\Delta f_{\mathrm{min}} > D_\alpha (\pi\ t^2_{\mathrm{chip}})^{-1}$ must be accomplished. Within this frequency range, the following two Δf values have been selected: one corresponding to a high Δf value (i.e., 1013 Hz) close to Δf_{max} with a low signal to noise ratio , and another one with a low Δf value (i.e., 113 Hz) close to Δf_{min} with a high signal to noise ratio. Notice that the FoM's or other IC parameters are not Δf dependent; therefore both scenarios should provide the same results.

D. Experimental set-up used in IR-LIT measurements

Fig. 4 depicts, placed on top of an optical breadboard, all elements involved in the IR-LIT measurements: the RF board, IR-Camera with its microscopic lens, and a heating micropositioning stage. Fig. 4 (a) displays the IR-LIT system mounted on top of a translational system and the RF board fixed onto the heating micro-positioning stage. Fig. 4 (b) provides a closer zoom to the RF and auxiliary boards, also highlighting

several parts of the heating micro-positioning stage.

This stage presents five degrees of freedom (X-Y-Z positioning, rotation and tilt), and imposes to the PA an operating temperature (T_i). In the performed measurements, T_i is set for 60ºC to prevent DC bias and small-signal models change from ambient thermal fluctuations and increase the IR-LIT system sensitivity. As for the stage parts, the sample micro-positioning one is implemented with an assembly of the following LINOS stages: the linear TL65 (Z axis, 1 µm sensitivity) and XY85 (X and Y axis, 1 µm sensitivity), the rotatory RT90 (rotation, 5s sensitivity) and the Goniometer 60-80 (tilting, 1 min sensitivity). On the other hand, the PA heating is carried out with a Linkam PE120 Peltier stage [see Fig. 4(b)] adjusted in closed loop with a Linkam T95-PE controller, which follows a PID approach. The PE120 is based on a water cooled Peltier cell soldered on top of the ends of a tinned aluminum plate. The rest of the available surface is used to heating up samples by conduction. Between them, thermal grease is applied to improve the heat transfer. For the PE120 control, the reference temperature is measured with a PT100 sensor embedded in an indentation at the plate backside close to the middle, so as to properly carry out the closed loop regulation from -25ºC to 125ºC. Moreover, this plate ensures a uniform heating of the sample backside due to its outstanding thermal properties, which practically avoid thermal gradients.

IV. Results and Discussion

A. PA driving influence and transistor thermal interaction

To study the feasibility of the proposed approach, the driving technique and $\Delta T_{M_1,\Delta f}(r_{M_1})$ measurement viability have been deeply analyzed. With the SA, the impact of the driving strategy on the output power amplitude has been measured and contrasted under the following conditions. At T_i = 60ºC, a total input power amplitude for homodyne ($|P_{\text{in},f_0}|$) and heterodyne ($|P_{\text{in het}}|$) driving of -3 dBm has been set to ensure $|P_{\text{in},f_0}| = 2|P_{\text{in},f_k}|$. In turn, $|P_{\text{in},f_0}|$ =-10 dBm and T_i = 25ºC have been accounted as a reference for results assessment. Concretely, the data for $f_{\text{c,G}}$ = 440 MHz have been presented, as they correspond to the lowest 1-dB CP case. To make such results comparable, the output power amplitude $|P_x|$, where the subscript x indicating "out, f_0" (homodyne) or "Z_{L,f_k}" (heterodyne), has been normalized to its value at $f_{\text{c,G}}$ ($|P_{\text{x,max}}|$). Fig. 5 presents the $|P_x|/|P_{\text{x,max}}|$ spectrum ($|P_x| - |P_{\text{x,max}}|$ in dBs) for each IC Fig. 5 shows that for each IC driving strategy, $|P_{\text{in},f_0}|$ and T_i; the output power delivered to the load follows the same dependency. Hence, the PA operates under linear regime, even though being close to its 1-dB CP at $f_{\text{c,G}}$ = 440 MHz. Moreover, we can assume $P_{\text{int}} \approx 0$, as $|P_{\text{out},f_0}| \approx 2|P_{Z_L,f_k}|$ and $|\Gamma_{\text{hom},f_0}| \approx |\Gamma_{\text{het},f_k}|$ holds. This makes the study easier, not requiring to compute $|P_{\text{int}}|/|P_{\text{in},f_0}|$ for FOM's extraction. This allows presenting all the results as a function of $|P_{Z_L,f_k}|$ and $|\Gamma_{\text{het},f_k}|$ instead of $|P_{\text{out},f_0}|$ and $|\Gamma_{\text{hom},f_0}|$. In any case, the approach is generic and applicable when $|P_{\text{int}}|/|P_{\text{in},f_0}| \neq 0$.

To check whether $\Delta T_{M_1,\Delta f}(r_{M_1})$ can be extracted; the contribution of each transistor to $|\Delta T|_{\text{tot},\Delta f}(r_{M_1}, r_{M_2})$ has been investigated. Fig. 6 depicts the $|\Delta T|_{\text{tot},\Delta f}(r_{M_1}, r_{M_2})$ images measured at Δf = 1013 Hz and $f_{\text{c,G}}$ = 440 MHz for several f_0's (300, 400, 440, 700 MHz). It can be observed that M_2 is the main heat source at f_0 = 300 MHz [Fig. 6 (a)] as no electrical power is delivered to Z_L up to 350 MHz, since C_{ext2} acts as a high pass filter. At higher frequencies [Figs. 6 (b) - 6(d)], M_1 starts the amplification following the low pass response of $\mathcal{H}_f$, and remains as the main heat source along the rest of the spectrum. At $f_0 = f_{\text{G,c}}$ [Fig. 6 (c)], both transistors heats up, as the maximum transfer of electrical power between input and output is ensured. Additionally M_1 dissipates its maximum power. The same behavior is observed when $f_{\text{c,G}}$ = 620 MHz. Thus, due to the PA's layout and inherent operation, for f_0 and f_k around $f_{\text{c,G}}$ $|\Delta T|^{M_1}_{\text{tot},\Delta f} = |\Delta T|_{\text{tot},\Delta f}(r_{M_1} = 0, r_{M_2} = d) \approx |\Delta T|_{M_1,\Delta f}(r_{M_1} = 0)$, whereas $\Delta T^{M_2}_{\text{tot},\Delta f} = \Delta T_{\text{tot},\Delta f}(r_{M_1} = d, r_{M_2} = 0) = \Delta T_{M_1,\Delta f}(r_{M_1} = d) + \Delta T_{M_2,\Delta f}(r_{M_2} = 0)$, where d is the distance between M_1 and M_2 (see Fig. 2). Therefore, $\Delta T_{M_1,\Delta f}(r_{M_1})$ can be inferred from $|\Delta T|_{\text{tot},\Delta f}(r_{M_1}, r_{M_2})$ in any PA cascode.

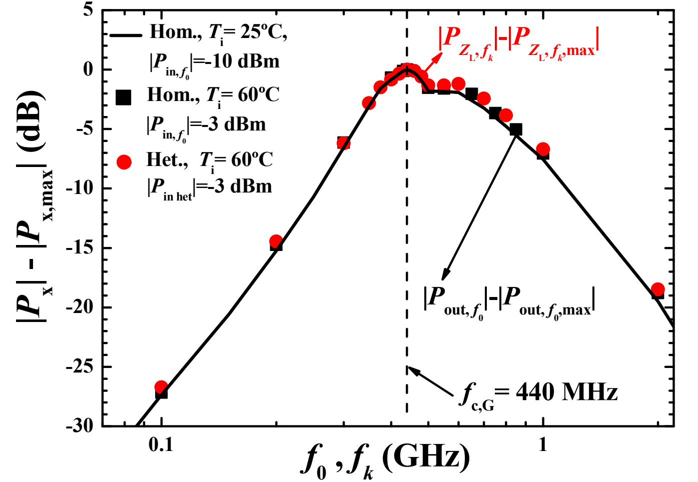

Fig. 5. $|P_x|$ normalized to $|P_{\text{x,max}}|$ when homodynally ($|P_{\text{out},f_0}|$ in black) and heterodynally ($|P_{Z_L,f_k}|$ in red) driven at $f_{\text{c,G}}$ = 440 MHz.

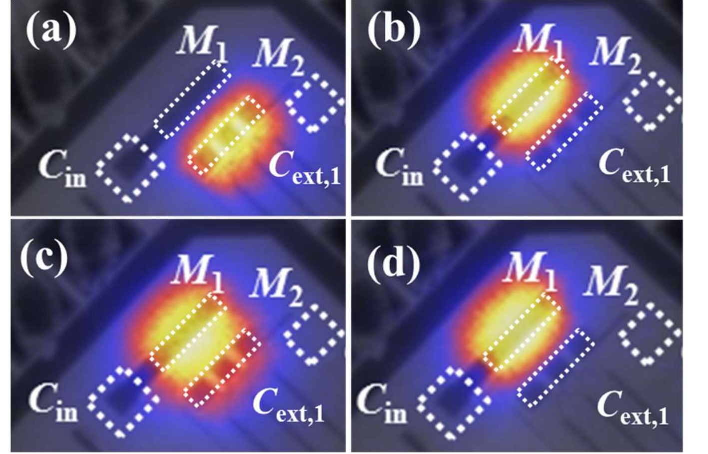

Fig. 6. $|\Delta T|_{\text{tot},\Delta f}(r_{M_1}, r_{M_2})$ measured at Δf = 1013 Hz and $f_{\text{c,G}}$ = 440 MHz, showing the heat sources M_1 and M_2 at several f_0's: (a) 300 MHz, (b) 400 MHz, (c) 440 MHz, and (d) 700 MHz (not at the same scale).

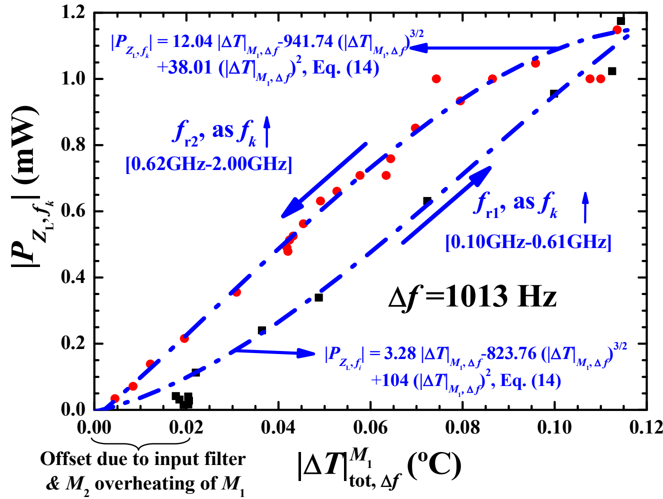

Fig. 7. Non-linear calibration curves for $|P_{Z_L,f_k}|$ when $f_{c,G}$ = 620 MHz and Δf = 1013 Hz for f_k ranging: i) f_{r1} defined from 100 to 620 MHz (in black), and ii) f_{r2} defined from 620 to 2000 MHz (in red). In blue, (16) fitting to experimental results are detailed.

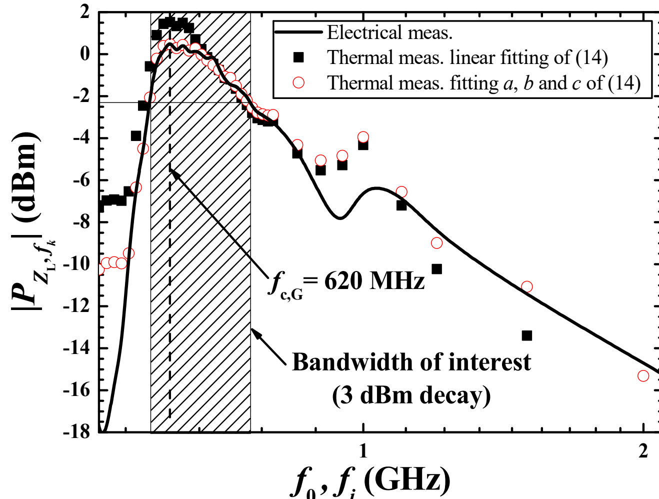

Fig. 8. Comparison between electrical (line) and thermal (points) measurements of $|P_{Z_L,f_k}|$, where M_1 is monitored fitting (16) assuming $b = c = 0$ (black squares) or $b \neq 0$ and $c \neq 0$ (green triangles).

B. $|P_{Z_L,f_k}|$ and M_2 behavior thermally monitored at M_1

According to IV.A results (i.e., $|\Delta T|^{M_1}_{\text{tot},\Delta f} \approx |\Delta T|_{M_1,\Delta f}\left(r_{M_1}=0\right)$), M_2 behavior and $|P_{Z_L,f_k}|$ have been derived from $|\Delta T|^{M_1}_{\text{tot},\Delta f}$ measurements far below the PA 1-dB CP. To inspect M_2 non-linear effects, $|P_{Z_L,f_k}|$ has been related with $|\Delta T|^{M_1}_{\text{tot},\Delta f}$ by fitting (16) in two ways. First, $a \neq 0$ and $b = c = 0$ have been considered to linearize (16), whereas in a second step, $a \neq 0$ $b \neq 0$ and $c \neq 0$ have been regarded. In both cases, all data pairs ($|P_{Z_L,f_k}|$, $|\Delta T|^{M_1}_{\text{tot},\Delta f}$) have been acquired at several f_k's and memoryless coefficients assumed for each f_{ri} [42], [43].

As an example, Fig. 7 depicts a non-linear fit (i.e., $a \neq 0$ $b \neq 0$ and $c \neq 0$) for $f_{c,G}$ = 620 MHz, $|P_{\text{in},f_0}| = |P_{\text{in het}}|$ = -5 dBm and Δf = 1013 Hz (blue dash-dotted line). Data pairs in black bold squares correspond to those whose f_k is between 100 MHz and $f_{c,G}$ (f_{r1}, $|\Delta T|^{M_1}_{\text{tot},\Delta f}$ increases), whereas red bold circles render those whose f_k ranges from $f_{c,G}$ to 2 GHz (f_{r2}, $|\Delta T|^{M_1}_{\text{tot},\Delta f}$ decreases). As a first observation, (16) fitting perfectly agrees with experimental results; where a, b, and c depend on f_{r1} and f_{r2}. In fact, (16) fitting and experimental results slightly differ for the lowest (black bold square) and the highest values (mainly in red bold circles) of $|\Delta T|_{M_1,\Delta f}(r_{M_1}=0)$. For the lowest values case, $|v_{sg2,f_k}|$ is constant as follows the low pass response of $\mathcal{H}_{f_k}$; while M_2 heats up M_1 due to $|\Delta T|_{M_1,\Delta f}\left(r_{M_1}=0\right) \ll |\Delta T|_{M_2,\Delta f}\left(r_{M_2}=d\right)$ (see Fig. 6), making difficult to extract $|\Delta T|_{M_1,\Delta f}(r_{M_1}=0)$ from $|\Delta T|^{M_1}_{\text{tot},\Delta f}$. When the highest values of $|\Delta T|_{M_1,\Delta f}(r_{M_1}=0)$ are considered (i.e., f_k close to $f_{c,G}$), the predicted and measured data disagree due to parasitic effects at the PA output, not taken into account in a, b, and c (memoryless coefficients). As for M_2 operation regime determination, experimental results within f_{r2} report a non-linear trend for $|P_{Z_L,f_k}|$ due only to $\mathcal{F}(v_{sg2})$, as ratified by the fitting excellent agreement. To deepening into this, Fig. 8 compares SA results for $|P_{Z_L,f_k}|$ with those inferred from $|\Delta T|^{M_1}_{\text{tot},f=\Delta f}$. Equation (16) closely fits electrical measurements, whereas in the linear case (i.e., $b = c = 0$), (16) partially reproduces $|P_{Z_L,f_k}|$ with a maximum error of about 2 dBm in the bandwidth indicated in Fig. 8. Such an error corresponds to a factor of 1.6 in a linear scale and, hence, a relative error of 60%. In the case of $f_{c,G}$=440 MHz, the same satisfactory results are obtained. Thus, taking $b \neq 0$ and $c \neq 0$ in (16) allows a fine data description, $|P_{Z_L,f_k}|$ monitoring, and M_2 behavior assessment.

C. $|\Gamma_{\text{het},f_k}|$ and M_2 behavior extracted at M_1 and M_2

The thermal monitoring of M_2 operation regime and $|\Gamma_{\text{het},f_k}|$ has been faced at M_1 and M_2 locations. $|\Gamma_{\text{het},f_k}|$ has been deduced from $|\Delta T|^{M_1}_{\text{tot},\Delta f}$ and $|\Delta T|^{M_2}_{\text{tot},\Delta f}$ measurements, where $|P_{\text{in},f_0}|$ and $|P_{\text{in het}}|$ are tuned slightly and far below the PA 1-dB CP. With this, M_2 non-linear effects can be checked in a wide input power range. Therefore, $|P_{\text{in},f_0}|$ and $|P_{\text{in het}}|$ have been set for -3 dBm at $f_{c,G}$ = 440 MHz and -5 dBm at $f_{c,G}$ = 620 MHz. Similarly to IV.B, $|\Gamma_{\text{het},f_k}|$ has been expressed in terms of $|\Delta T|^{M_1}_{\text{tot},\Delta f}$ and $|\Delta T|^{M_2}_{\text{tot},\Delta f}$ by fitting (20). Fig. 9 depicts the $|\Gamma_{\text{het},f_k}|$ response extracted from electrical and $|\Delta T|^{M_1}_{\text{tot},\Delta f}$ measurements for the accounted $f_{c,G}$'s [620 and 440 MHz, (a) and (b), respectively] and Δf's (1013 and 113 Hz), demonstrating an excellent matching between them. Electrical and thermal results mainly diverge in Fig. 9 (a) (second resonance peak) due to parasitic effects when electrically measured, but not thermally. Thus, thermally-inferred $|\Gamma_{\text{het},f_k}|$ is not dependent on 1-dB CP, $f_{c,G}$ and Δf, as M_2 exhibits non-linear effects regardless of $|P_{\text{in},f_0}|$.

As for $\Delta T_{M_1,\Delta f}\left(r_{M_1}\right)$ measurements at M_2 location (i.e., $r_{M_1}=d$), Fig. 10 displays $|\Gamma_{\text{het},f_k}|$ versus $|\Delta T|^{M_1}_{\text{tot},\Delta f}$ and

$|\Delta T|^{M_2}_{\mathrm{tot},\Delta f}$ when $|P_{\mathrm{in},f_0}| = |P_{\mathrm{in\ het}}|$ = -3 dBm, $f_{\mathrm{c,G}}$ = 440 MHz and Δf = 1013 Hz. In this case, three frequency ranges (f_{r1}, f_{r2}, and f_{r3})have been considered to account for all memoryless behaviors. $|\Delta T|^{M_1}_{\mathrm{tot},\Delta f}$ has been acquired regarding single pixel (sensor 1 location and in the middle of M_2) and area-averaged (M_1 and M_2) thermal measurements (see Fig. 10 inset). Fig. 10 shows that $|\Delta T|^{M_1}_{\mathrm{tot},\Delta f}$ and $|\Delta T|^{M_2}_{\mathrm{tot},\Delta f}$ behave alike, and $|\Delta T|^{M_2}_{\mathrm{tot},\Delta f} \approx |\Delta T|_{M_1,\Delta f}\,(r_{M_1} = d)$ holds. Thus, $|\Gamma_{\mathrm{het},f_k}|$ spectrum and M_2 operation can be inferred from $|\Delta T|^{M_2}_{\mathrm{tot},\Delta f}$ after (20) fitting. To highlight this, Fig. 11 compares all electrical and thermal results for $|\Gamma_{\mathrm{het},f_k}|$ extraction considering several $f_{\mathrm{c,G}}$'s (440 and 620 MHz) and Δf's (113 and 1013 Hz). The effect of inspecting areas [see Fig. 11 (a)] or pixels [see Fig. 11 (b)] in the thermal image is also depicted. In both cases, thermal results perfectly agree with electrical data. More oscillatory [see Fig. 11 (a)] or abrupt [see Fig. 11 (b)] patterns are observed in the electrical measurements due to parasitics introduced by the board and wiring in $\mathcal{H}_f$ (non-considered in Fig. 3) and $Z_{\mathrm{o},f}$ (due mainly to $Z_{\sigma,f}$), which do not affect thermal inspections. After a previous calibration with (20), sensor 1 measurements at Δf = 1013 Hz are included in Fig. 11 (b), depicting an excellent matching with all thermal results. Moreover, Fig. 11 points to that $|\Gamma_{\mathrm{het},f_k}|$ is independent from acquiring thermal data in averaged-areas, pixels, transistor, or any value for Δf, as long as the signal to noise ratio would be optimum. Moreover, placing a thermal sensor in M_2 could be a good solution to thermally determine $|P_{Z_{\mathrm{L}},f_k}|$ and $|\Gamma_{\mathrm{het},f_k}|$ in a narrow frequency range around $f_{\mathrm{c,G}}$, but not for monitoring their whole spectrum. Fortunately, this range is wide enough for $\mathcal{F}(v_{sg2,f})$ behavior assessment.

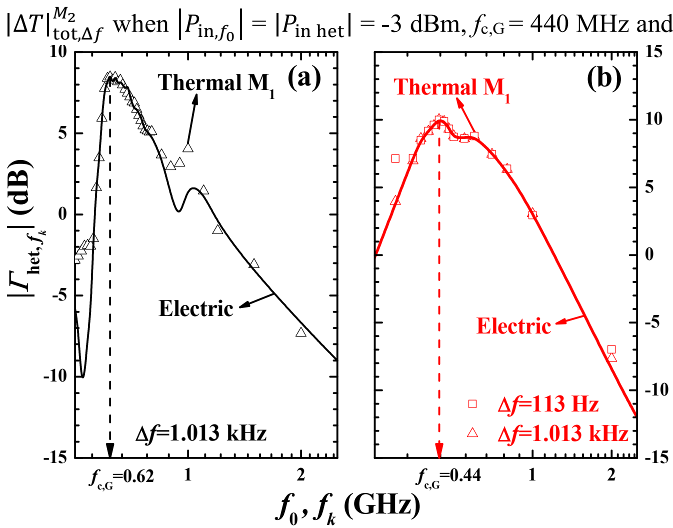

Fig. 9. Comparison of $|\Gamma_{\mathrm{het},f_k}|$ when extracted by electrical and thermal means at M_1 for several $f_{\mathrm{c,G}}$'s: a) $f_{\mathrm{c,G}}$ = 620 MHz and Δf = 1013 Hz, b) $f_{\mathrm{c,G}}$ = 440 MHz and various Δf's (113 and 1013 Hz).

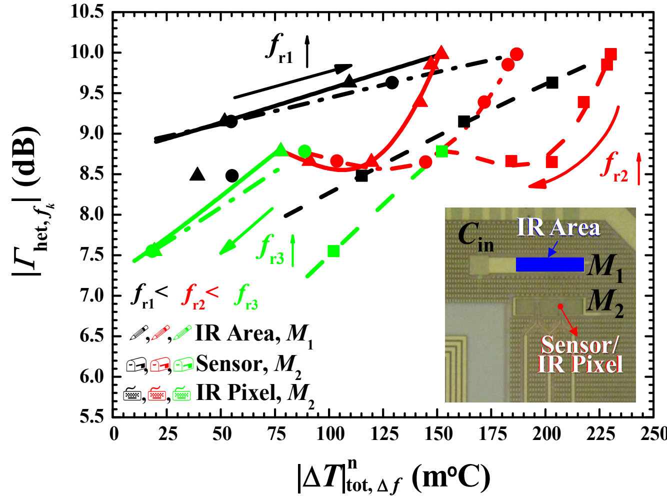

Fig. 10. Comparison of calibration results for M_1 and M_2 (given by n) when $f_{\mathrm{c,G}}$=440MHz and Δf = 1013 Hz, considering pixels or areas for the ranges f_{r1}, f_{r2}, and f_{r3}. The inset shows the areas and pixels accounted, also denoting the colors assigned in the graph.

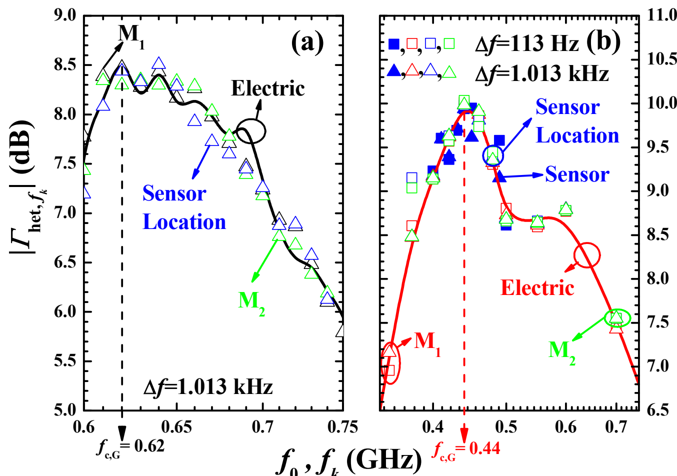

Fig. 11. Comparison of electrical and thermal results for power gain determination when: a) $f_{\mathrm{c,G}}$ = 620 MHz, Δf = 1013 Hz, and inspecting areas in M_1 and M_2; b) $f_{\mathrm{c,G}}$ = 440 MHz, accounting for several Δf's (113 and 1013 Hz), and considering central pixels in M_1 and M_2.

V. Conclusions

As an innovation to the mainstream approaches, the use of IR-LIT has been proved to extract FoM's and transistors operation regimes in RF PA's. The study has been focused on a Class A RF PA (with different central frequencies) by extracting both the output power and the power gain in the range from 100 MHz to 2 GHz. Moreover, the operation regime of their transistors has been deeply analyzed. To carry out this, the PA has been heterodinally driven to downconvert such a high frequency information into a lower one within the IR-LIT system bandwidth. To explore the approach feasibility, a theoretical analysis has been performed on the basis of a small-signal equivalent circuit and analytical expressions. Such a model relates the PA FoM's and transistors operation with the thermal field $\Delta T_{\mathrm{tot},\Delta f}$, taking into account the PA frequency behavior and a non-constant transconductance $\mathcal{F}(v_{sg2,f})$ in M_2. As a calibration procedure, such a model has been fitted to all experimental data with an excellent agreement, pointing to several conclusions. Firstly, $|\Delta T|^{M_1}_{\mathrm{tot},\Delta f}$ has been identified as the best candidate for testing the transistors operation regimes, output power, and power gain. Secondly, $|\Delta T|^{M_2}_{\mathrm{tot},\Delta f}$ is also

suitable in a reduced spectral range, in which $|\Delta T|_{\text{tot},\Delta f}^{M_2} \approx |\Delta T|_{M_1,\Delta f}(r_{M_1} = d)$ holds. Thirdly, M_2 manifests short channel and vertical field effects along the analyzed spectral range regardless of the PA input power.

As other applications, the proposed approach can be applied to $f_{c,G}$ or amplifier bandwidth determination for dependability studies in cascode PA's or other single-transistor topologies. Moreover, thermal imaging may become a breakthrough to assess the best location for MIC's integration in SoC's.

REFERENCES

[1] A. M. Nikinejad, D. Chowdhury, and J. Chen, "Design of CMOS Power Amplifiers", *IEEE Trans. Microw. Theory Techn.*, vol. 60, DOI: 10.1109/TMTT.2012.2193898, no. 6, pp. 1784-1796, May 2012.

[2] M. Lee, C. Lee and C. Park, "Transceiver for Wireless Power Transfer Using a Cross-Coupled Oscillator for a Wireless On-Wafer Test," IEEE Trans. Instrum. and Meas., vol. 66, DOI: 10.1109/TIM.2017.2677658no. 8, pp. 2097-2105, Aug. 2017.

[3] S. R. Helmi, J. H. Chen, and S. Mohammadi, "A stacked Cascode CMOS SOI power amplifier for mm-wave applications," in *Proc. of IEEE MTT-S International Microwave Symposium* (*IMS*), (Tampa, USA), DOI: 10.1109/ MWSYM.2014.6848589, pp. 1-3, Jun. 2014.

[4] J. H. Chen, S. R. Helmi, R. Azadegan, F. Aryanfar, and S. Mohammadi, "A Broadband Stacked Power Amplifier in 45-nm CMOS SOI Technology," *IEEE J. Solid-State Circuits*, vol. 48, DOI: 10.1109/JSSC.2013.2276135, no. 11, pp. 2775-2784, Aug. 2013.

[5] J. Y. Hasani, "Design of a Radiofrequency Front-End module for Smart Dust sensor network". PhD dissertation, Université Joseph-Fourier, Grenoble, 2008.

[6] M. Tadeusiewicz and S. Hałgas, "A Method for Local Parametric Fault Diagnosis of a Broad Class of Analog Integrated Circuits," *IEEE Trans. Instrum. Meas.*, vol. 67, DOI: 10.1109/TIM.2017.2775438, no. 2, pp. 328-337, Feb. 2018.

[7] A. Valdes-Garcia, R. Venkatasubramanian, J. Silva-Martinez, and E. Sánchez-Sinencio, "A broadband CMOS amplitude detector for on-chip RF measurements," *IEEE Trans. Instrum. Meas.*, vol. 57, DOI: 10.1109/TIM.2008.917196, no. 7, pp. 1470–1477, July 2008.

[8] H. W. Ting, "A Digital Testing Strategy for Characterizing an Analog Circuit Block," *IEEE Trans. Instrum. Meas.*, vol. 65, DOI: 10.1109/TIM.2016.2534298, no. 6, pp. 1374-1384, June 2016.

[9] J. Altet, D. Gomez, X. Perpiñà, D. Mateo, J.-L. González, M. Vellvehi, and X. Jordà, "Efficiency determination of RF linear power amplifiers by steady-state temperature monitoring using built-in sensors," *Sens. Actuator A-Phys.*, vol. 192, DOI: 10.1016/j.sna.2012.12.010, no. 4, pp. 49-57, Apr. 2013.

[10] M. Azimane, "Reducing Test Cost for Mixed Signal Circuits "From TOETS to ELESIS", in *Proc. of IEEE European Test Symposium* (*ETS*), DOI: 10.1109/ETS.2012.6233051 (Annecy, France), May 2012.

[11] Q. Yin, W.R. Eisenstadt, R.M. Fox, and T. Zhang, "A translinear RMS detector for embedded test of RF ICs," *IEEE Trans. Instrum. Meas*., vol. 54, DOI: 10.1109/TIM.2005.855105, no. 5, pp. 1708-1714, Oct. 2005.

[12] A. Valdes-Garcia, F. A. L. Hussien, J. Silva-Martinez, E. Sánchez-Sinencio, "An integrated frequency response characterization system with a digital interface for analog testing", *IEEE J Solid-State Circuits*, vol. 41, DOI: 10.1109/JSSC.2006.881561, no. 10, pp. 2301-2313, Oct. 2006.

[13] S. Bhattacharya, A. Chatterjee, "Use of embedded sensors for built-in-test RF circuits", in *Proc IEEE International Test Conference* (ITC), DOI: 10.1109/TEST.2004.1387343, (Charlotte, USA), pp 801-809, Oct. 2004.

[14] C. Azcona, B. Calvo, N. Medrano and S. Celma, "1.2 V–0.18- μm CMOS Temperature Sensors With Quasi-Digital Output for Portable Systems," *IEEE Trans. Instrum. Meas.*, vol. 64, DOI: 10.1109/TIM.2015.2408804, no. 9, pp. 2565-2573, Sept. 2015.

[15] M. Onabajo, D. Gómez, E. Aldrete-Vidrio, J. Altet, D. Mateo, J. Silva-Martínez, "Survey of Robustness Enhancement Techniques for Wireless Systems-on-a-Chip and Study of Temperature as Observable for Process Variations", *Journal of Electronic Testing*, vol. 27, DOI: 10.1007/s10836-011-5199-6, no. 3, pp. 225-240, Jun. 2011.

[16] F. Reverter and J. Altet, "On-chip thermal testing Using Mosfets in Weak Inversion," *IEEE Trans. Instrum. Meas.*, vol. 64, DOI: 10.1109/TIM.2014.2341371, no. 6, pp. 524-532, Feb. 2015.

[17] S. Y. Suck, G. Tessier, N. Warnasooriya, A. Babuty, and Y. De Wilde, "Frequency-resolved temperature imaging of integrated circuits with full field heterodyne interferometry," *Appl. Phys. Lett.*, vol. 96, DOI: 10.1063/1.3367738, no. 12, pp. 121108, Mar. 2010.

[18] L. Aigouy, G. Tessier, M. Mortier, and B. Charlot, "Scanning thermal imaging of microelectronic circuits with a fluorescent nanoprobe", *Appl. Phys. Lett.*, vol. 87, DOI: 10.1063/1.2123384, no. 18, pp. 184105, Oct. 2005.

[19] J. León, X. Perpiñà, M. Vellvehi, A. Baldi, J. Sacristán, and X. Jordà, "Wireless pad-free integrated circuit debugging by powering modulation and lock-in infrared sensing", *Appl. Phys. Lett.*, vol. 102, DOI: 10.1063/1.4793665, no. 8, pp. 084106, Feb. 2013.

[20] M. Bâzu, and T. Băjenescu, Failure Analisis: A practical guide for Manufacturers of electronic components and systems, Wiley series in Quality and reliability engineering, Chichester (UK): Wiley, Apr. 2011, vol. 7, ch. 4, pp. 71–108.

[21] X. Perpiñà, X. Jordà, M. Vellvehi, and J. Altet, "Hot spot analysis in integrated circuit substrates by laser mirage effect", *Appl. Phys. Lett.*, vol. 98, DOI: 10.1063/1.3581038, no. 16, no. 164104, Mar. 2011.

[22] J. León, X. Perpiñà, J. Sacristan, M. Vellvehi, A. Baldi, X. Jordà, "Functional and consumption analysis of integrated circuits supplied by inductive power transfer by powering modulation and lock-in infrared imaging," *IEEE Trans. on Ind. Electron.*, Vol. 62, DOI: 10.1109/TIE.2015.2455024, no. 12, pp. 7774-7785, Dec. 2015.

[23] J. León, X. Perpiñà, J. Altet, M. Vellvehi, and X. Jordà, "Physically based analysis of electrical frequency response of passive microelectronic circuits by heterodyne lock-in thermal means," *J. Phys. D Appl. Phys.*, vol. 46, DOI: 10.1088/0022-3727/46/44/445501, no. 44, pp. 445501, Oct. 2013.

[24] E. Aldrete-Vidrio, D. Mateo, J. Altet, M. A. Salhi, S. Grauby, S. Dilhaire, M. Onabajo, and J. Silva-Martinez, "Strategies for built-in characterization testing and performance monitoring of analog RF circuits with temperature measurements" *Meas. Sci. Technol.*, vol. 21, DOI: 10.1088/0957-0233/21/7/075104, no. 7, 075104, June 2010.

[25] J. Altet, D. Mateo, D. Gómez, J. L. González Jiménez, B. Martineau, A. Siligaris, X. Aragones, "Temperature Sensors to Measure the Central Frequency and 3 dB Bandwidth in mmW Power Amplifiers," in *IEEE Microw. Compon. Lett.*, vol. 24, DOI: 10.1109/LMWC.2013.2293668, no. 4, pp. 272-274, Apr. 2014.

[26] A. Shakouri, "Nanoscale Thermal Transport and Microrefrigerators on a Chip," *P. IEEE*, vol. 94, DOI: 10.1109/JPROC.2006.879787, no. 8, pp. 1613-1638, Aug. 2006.

[27] S. Stipetic, M. Kovacic, Z. Hanic, and M. Vrazic, "Measurement of Excitation Winding Temperature on Synchronous Generator in Rotation Using Infrared Thermography", *IEEE Trans. Ind. Electron.*, vol. 59, DOI: 10.1109/TIE.2011.2158047, no. 5, pp. 2288-2298, May 2012.

[28] E. Imaz, R. Alonso, C. Heras, I. Salinas, E. Carretero, and C. Carretero, "Infrared Thermometry System for Temperature Measurement in Induction Heating Appliances", *IEEE Trans. Ind. Electron.*, vol. 61, DOI: 10.1109/TIE.2013.2281166, no. 5, pp. 2622-2630, May 2014.

[29] J. C. Olivares-Galván, S. Magdaleno-Adame, R. Escarela-Pérez, R. Ocón-Valdez, P. S. Georgilakis, and G. Loizos, "Reduction of Stray Losses in Flange–Bolt Regions of Large Power Transformer Tanks", *IEEE Trans. Ind. Electron.*, vol. 61, DOI: 10.1109/TIE.2013.2279373, no. 8, pp. 4455-4463, Aug. 2014.

[30] O. Breitenstein, W. Warta, and M. Langenkamp, Lock-in thermography: Basics and Use for Evaluating Electronic Devices and Materials, 2nd ed. (Springer-Verlag Berlin Heidelberg, 2010).

[31] J. P. Rakotoniaina, O. Breitenstein, and M. Langenkamp, "Localization of weak heat sources in electronic devices using highly sensitive lock-in thermography", *Mater. Sci. Eng. B-Adv.,* vol. 91-92, pp. 481-485, Apr. 2002.

[32] X. Perpiñà, J. León, J. Altet, M. Vellvehi, F. Reverter, E. Barajas, X. Jordà, "Thermal phase lag heterodyne infrared imaging for current tracking in radio frequency integrated circuits", *Appl. Phys. Lett.*, no. 110, DOI: 10.1063/1.4977175, pp. 094101_1-094101_5, vol. 9, Feb. 2017.

[33] S. Arshad, F. Zafar, R. Ramzan, and Q. Wahab, "Wideband and multiband

CMOS LNA: State-of-art and future prospects", *Microelectron. J.*, vol. 44, DOI: 10.1016/j.mejo.2013.04.011, no. 9, pp. 774-786, Sept. 2013.

[34] A. S. Sedra and K. C. Smith, Chapter 6: Single-stage Integrated-Circuit Amplifiers, Section 6.8 The cascode amplifier, in Microelectronic Circuits, in the series: The Oxford Series in Electrical and Computer Engineering, pp. 618-620 (Oxford University Press, 5th ed., New York, 2004).

[35] P. E. Allen and D. R. Holberg, "Chapter 5: CMOS Amplifiers, Section 5.3: Cascode Amplifiers", in CMOS Analog Circuit Design, in the series: The Oxford Series in Electrical and Computer Engineering, pp. 199-211 (Oxford University Press, 2nd ed., New York, 2002.

[36] F. Reverter, J. Altet, "MOSFET temperature sensors for on-chip thermal testing," *Sens. Actuators A Phys.*, vol. 203, pp. 234-240, DOI: 10.1016/j.sna.2013.08.026, no. 12, Dec. 2013.

[37] F. Reverter, D. Gómez, and J. Altet, "On-chip MOSFET Temperature Sensor for Electrical Characterization of RF Circuits," *IEEE Sens. J.*, vol. 13, DOI: 10.1109/JSEN.2013.2273572, no. 9, pp. 3343-3344, sept. 2013.

[38] F. Reverter, X. Perpiñà, E. Barajas, J. León, M. Vellvehi, X. Jordà, J. Altet, "MOSFET dynamic thermal sensor for IC testing applications," *Sens. Actuators A Phys.*, vol. 242, DOI: 10.1016/j.sna.2016.03.0162016, no. 5, pp. 195-202, May 2016.

[39] M. T. Terrovitis, and Robert G. Meyer, "Intermodulation Distortion in Current-Commutating CMOS Mixers", *IEEE J. Solid-State Circuits*, vol. 35, DOI: 10.1109/4.871323, no. 10, Oct. 2000

[40] Bonkee Kim, Jin-Su Ko and Kwyro Lee, "A new linearization technique for MOSFET RF amplifier using multiple gated transistors," in *IEEE Microw. Compon. Lett.*, vol. 10, DOI: 10.1109/75.867854, no. 9, pp. 371-373, Sep. 2000

[41] J. León, Advanced Analysis of Microelectronic Devices and Systems by lock-in IR Thermography, Ph D Thesis dissertation, pp. 251, 2016.

[42] P. Jantunen, "Modelling of Nonlinear Power Amplifiers for Wireless Communications", Master of Science dissertation, Department of Electrical and Communications Engineering, Helsinki University of Technology, 2004.

[43] N. Wolf, J.-E. Mueller, H. Klar, "Identification of Frequency Dependent Memory Effects and the Linearization of a CMOS PA for Multiple Standards", in *Proc. of 11th IEEE Radio and Wireless Symposium* (*RWS*), DOI: 10.1109/RWS.2009.4957422, (San Diego, USA), Jan. 2009, pp. 598-601.

[44] M. Vellvehi, X. Perpiñà, G. L. Lauro, F. Perillo, and X. Jordà, "Irradiance-based emissivity correction in infrared thermography for electronic applications", *Rev. Sci. Instrum.*, vol. 82, DOI: 10.1063/1.3657154, no. 11, pp. 114901, Nov. 2011.

[45] X. Perpiñà, X. Jordà, M. Vellvehi, J. Altet, and N. Mestres, "Steady-state sinusoidal thermal characterization at chip level by internal infrared-laser deflection," *J. Phys. D Appl. Phys.*, vol. 41, DOI:10.1088/0022-3727/41/15/155508, no. 15, pp. 155508-1 – 155508-8, Jul. 2008.